PNAS RESEARCH ARTICLE | ENVIRONMENTAL SCIENCES

# Climatic and biotic factors influencing regional declines and recovery of tropical forest biomass from the 2015/16 El Niño

Hui Yang[a,1], Philippe Ciais[a], Jean-Pierre Wigneron[b], Jérôme Chave[c], Oliver Cartus[d], Xiuzhi Chen[e], Lei Fan[f], Julia K. Green[a], Yuanyuan Huang[g], Emilie Joetzjer[h], Heather Kay[i], David Makowski[j], Fabienne Maignan[a], Maurizio Santoro[d], Shengli Tao[c], Liyang Liu[a,e], and Yitong Yao[a]

Edited by Steven Wofsy, Harvard University, Cambridge, MA; received January 22, 2021; accepted April 4, 2022

**The 2015/16 El Niño brought severe drought and record-breaking temperatures in the tropics. Here, using satellite-based L-band microwave vegetation optical depth, we mapped changes of above-ground biomass (AGB) during the drought and in subsequent years up to 2019. Over more than 60% of drought-affected intact forests, AGB reduced during the drought, except in the wettest part of the central Amazon, where it declined 1 y later. By the end of 2019, only 40% of AGB reduced intact forests had fully recovered to the predrought level. Using random-forest models, we found that the magnitude of AGB losses during the drought was mainly associated with regionally distinct patterns of soil water deficits and soil clay content. For the AGB recovery, we found strong influences of AGB losses during the drought and of $\gamma$. $\gamma$ is a parameter related to canopy structure and is defined as the ratio of two relative height (RH) metrics of Geoscience Laser Altimeter System (GLAS) waveform data—RH25 (25% energy return height) and RH100 (100% energy return height; i.e., top canopy height). A high $\gamma$ may reflect forests with a tall understory, thick and closed canopy, and/or without degradation. Such forests with a high $\gamma$ ($\gamma \geq 0.3$) appear to have a stronger capacity to recover than low-$\gamma$ ones. Our results highlight the importance of forest structure when predicting the consequences of future drought stress in the tropics.**

tropical forest | drought | recovery | forest structure

## Significance

The 2015/16 El Niño led to a megadrought, impacting tropical forests. We used passive microwave observations to monitor the above-ground biomass (AGB) changes during and after the 2015/16 drought. Based on a statistical model, the pattern of AGB changes—mostly decreases—during the drought was found to be primarily associated with drought severity and duration, as well as with soil clay content. The pattern of AGB recovery was influenced jointly by previous AGB losses and by the canopy structure of forests. This highlights that, in addition to environmental factors, the resilience of forest communities to the 2015/16 droughts also depends upon forest structure. This should be better taken into account when anticipating the impacts of future droughts in the tropics.

Tropical forests hold the largest biomass pool on Earth and account for more than one-third of the total global net primary productivity (NPP) (1). Small changes in their growth and mortality rates can substantially affect their carbon balance, with a global impact on the growth rate of atmospheric $CO_2$ (2). The El Niño-Southern Oscillation leads to droughts impacting highly productive tropical forests, compounded with fires and increased pathogens and insect attacks (3), which enhance tree mortality and reduce carbon storage, weakening the tropical forest carbon sink (4, 5). Previous observational and modeling studies reported that tropical regions switched from a carbon sink to source as a result of drought associated with the severe El Niño event in 2015 to 2016 (6–8). However, few studies have explored the factors that control the spatial and temporal variations in forest carbon loss and gains during and subsequent recovery patterns.

The 2015/16 El Niño brought record-breaking temperatures and water deficits in the tropics. Warmer and drier conditions are close to those anticipated in future warming scenarios (9). Increases in the severity, duration, and frequency of drought and heat stress associated with climate change could fundamentally alter the community composition, structure, and biogeography of forests (10, 11). The recently available L-band microwave vegetation optical depth (L-VOD) observation allows us to monitor short-term and long-term responses of biomass to such a major climate disturbance by capturing above-ground biomass (AGB) changes with less saturation than other satellite-based proxies. The short-term response to drought is usually a decline in photosynthesis due to stomata closure and impaired hydraulic transport from soil-moisture declines, monitored through field and satellite observations during drought, except in some ever-wet regions, where enhanced radiation can locally increase photosynthesis or when drought is not too severe (12–14). The long-term response involves tree mortality, changes in forest structure, and recruitment, which persist for several years after drought (8, 15).

Using random forest (RF) models, a machine-learning algorithm, we identify here the key climatic, edaphic, and biotic factors controlling regional declines and subsequent recovery of biomass across intact tropical forests after the 2015/16 El Niño event. We use the large-scale Lidar observation of forest structure as a variable to help explain the postdrought biomass variations because legacy impacts of drought affect

Author contributions: H.Y., P.C., and J.-P.W. designed research; H.Y. and P.C. performed research; J.-P.W., O.C., and M.S. contributed new reagents/analytic tools; H.Y., J.C., J.K.G., Y.H., and D.M. analyzed data; and H.Y., P.C., J.-P.W., J.C., X.C., L.F., J.K.G., Y.H., E.J., H.K., D.M., F.M., S.T., L.L., and Y.Y. wrote the paper.

The authors declare no competing interest.

This article is a PNAS Direct Submission.



[1]To whom correspondence may be addressed. Email: huiyang.pku@gmail.com.

This article contains supporting information online at http://www.pnas.org/lookup/suppl/doi:10.1073/pnas.2101388119/-/DCSupplemental.

Published June 22, 2022.

not only mortality and growth of individual trees, but also recruitment and community composition (11).

## Results

**Severity, Duration, and Onset Timing of 2015/16 Drought.** We assess the extent and severity of the 2015/16 drought using the standardized anomaly of cumulative water deficits (ACWD) derived from monthly precipitation measured by the Tropical Rainfall Measuring Mission (TRMM) and evapotranspiration (ET) from the Global Land Evaporation Amsterdam Model (GLEAM) (16) (*Materials and Methods*). We focus on the tropical intact evergreen forests, using a conservative intact forest-cover mask to avoid misclassification of drought over nonforested or anthropogenic disturbance-affected regions (*Materials and Methods*). After mid-2015, more than 55% of tropical intact evergreen forests in South America (2.53 million $km^2$), 34% in Africa (0.40 million $km^2$), and 42% in Southeast Asia (0.19 million $km^2$) were exposed to ACWD $< -1$ SD for more than 3 mo (the SD being for the period 2010 through 2019 when satellite AGB data are available). The patterns shown in Fig. 1 illustrate the severity (Fig. 1*A*), duration (Fig. 1*B*), and onset time (Fig. 1*C*) of the 2015/16 drought. The drought first hit Southeast Asia, then Africa and South America (Fig. 1*C*). Drought duration and severity differed spatially, and the areas under more severe drought tended to have a longer-lasting exposure. The epicenter of drought was in central Amazonia, where rainforests experienced ACWD $< -2$ SD for more than 8 mo. By contrast, the drought was less severe in eastern Amazonia and in most parts of Africa and was relatively short-lasting (less than 6 mo) in western Africa and Southeast Asia. Note that using the Moderate Resolution Imaging Spectroradiometer (MODIS) ET product instead of GLEAM to calculate ACWD gives similar patterns of drought severity and duration (*SI Appendix*, Fig. S1).

**Changes in AGB During and After Drought.** We examine the impact of 2015/16 drought on forest AGB using L-VOD remote-sensing data from the Soil Moisture and Ocean Salinity (SMOS) satellite (17). L-VOD may respond not only to vegetation, but also to vegetation water-content dynamics (18). In order to remove a possible contribution of vegetation water-content variation to vegetation optical depth (VOD) changes, we use multiple regressions of VOD against the normalized difference water index (a proxy of water content of whole plant) and the normalized difference vegetation index (a proxy of vegetation-leaf biomass) (see details in *SI Appendix*, Text S1 and Fig. S2). The similar results of L-VOD AGB changes without and with correction for water content (*SI Appendix*, Fig. S3) confirm that the year-to-year changes in L-VOD mainly reflect changes in AGB, being slightly affected by changes in water content on interannual scales.

Changes in AGB stocks during the 2015/16 drought period, relative to the same period during the predrought year ($\Delta AGB_{14/15\rightarrow 15/16}$; see *Materials and Methods* for the definition of this notation) are calculated for 25-km pixels over tropical intact evergreen forests exposed to drought. The results shown in Fig. 2*A* indicate an immediate AGB reduction during the 2015/16 drought period over more than 60% of drought-affected intact forests, particularly in southeastern Amazonia and in Africa and Borneo of Southeast Asia. One exception is the "ever-wet" rainforest region of central Amazonia, which showed an increase in AGB during the drought. Previous studies observed lagged tree mortality after drought, yet with no significant reduction in the growth of surviving trees, e.g., at the Caxiuanã rainfall exclusion experiment (19) and at ecological monitoring sites in the Amazon during the 2010 drought (20), as well as for in a variety of tree genera globally (21). The lack of suppressed tree growth or enhanced growth during the drought in the ever-wet part of the Amazon may be due to sustained canopy photosynthetic capacity (22, 23) from greater radiation availability (24), coordinated with the flushing of young and more efficient leaves in the early drought stages (25, 26) and higher vapor pressure deficit (VPD), resulting in an increase of water-use efficiency offsetting the regulation of stomatal closure, leading to a net increase of canopy photosynthesis (27).

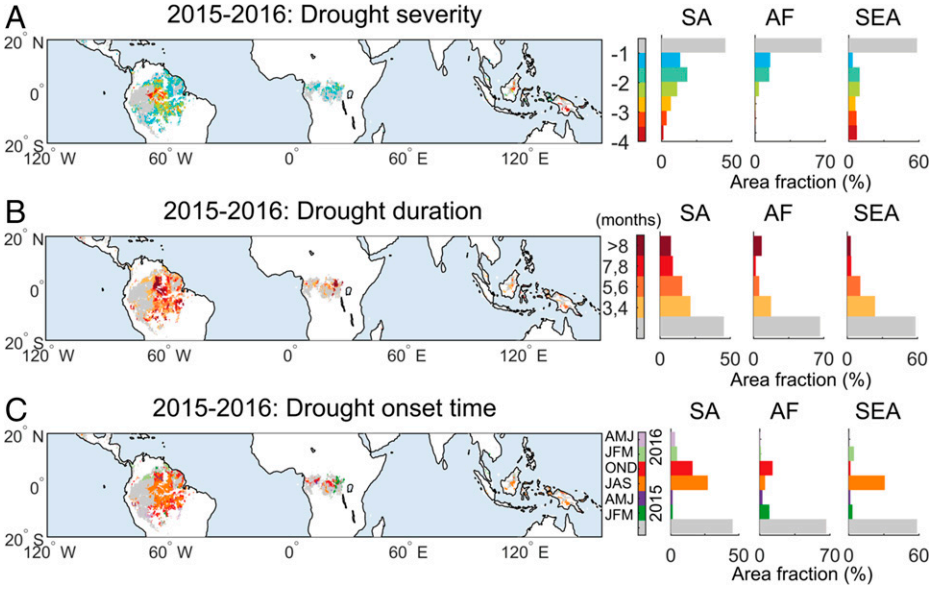


**Fig. 1.** Spatial patterns of the severity (*A*), duration (*B*), and onset timing (*C*) of the 2015/16 drought over the tropical evergreen forests. The severity, duration, and onset of drought are identified based on the ACWD. *Left* shows the fractional area of tropical forests sorted into different categories of drought severity, duration, and onset timing. In penal C, JFM represents January, February, March; AMJ represents April, May and June; JAS represents July, August and September, OND represents October, November and December. The fractional area is split into values for three continents, i.e., South America (SA), Africa (AF), and Southeast Asia (SEA). The gray areas are the areas where the ACWD is greater than −1 (i.e., non-drought-affected region). The non-forest-dominated regions, forest-losses regions, flooded, and lake areas are masked out.

The postdrought trajectories of AGB are shown in Fig. 2 *B* and *C*, revealing complex patterns that differ among regions. On the one hand, a lagged and persistent decrease in AGB was observed after the termination of the 2015/16 drought in north-central and eastern Amazonian and western Congo forests (Fig. 2*B*), despite the gradual recovery of rainfall and no new drought event (*SI Appendix*, Fig. S4). The occurrence of fires in subsequent years—in particular, during 2017/18—may be partly responsible for additional AGB reductions after the drought—for example, in the eastern Amazon (*SI Appendix*, Fig. S5). A lagged decrease of AGB is consistent with findings based on satellite laser altimeter data of a lagged loss of height

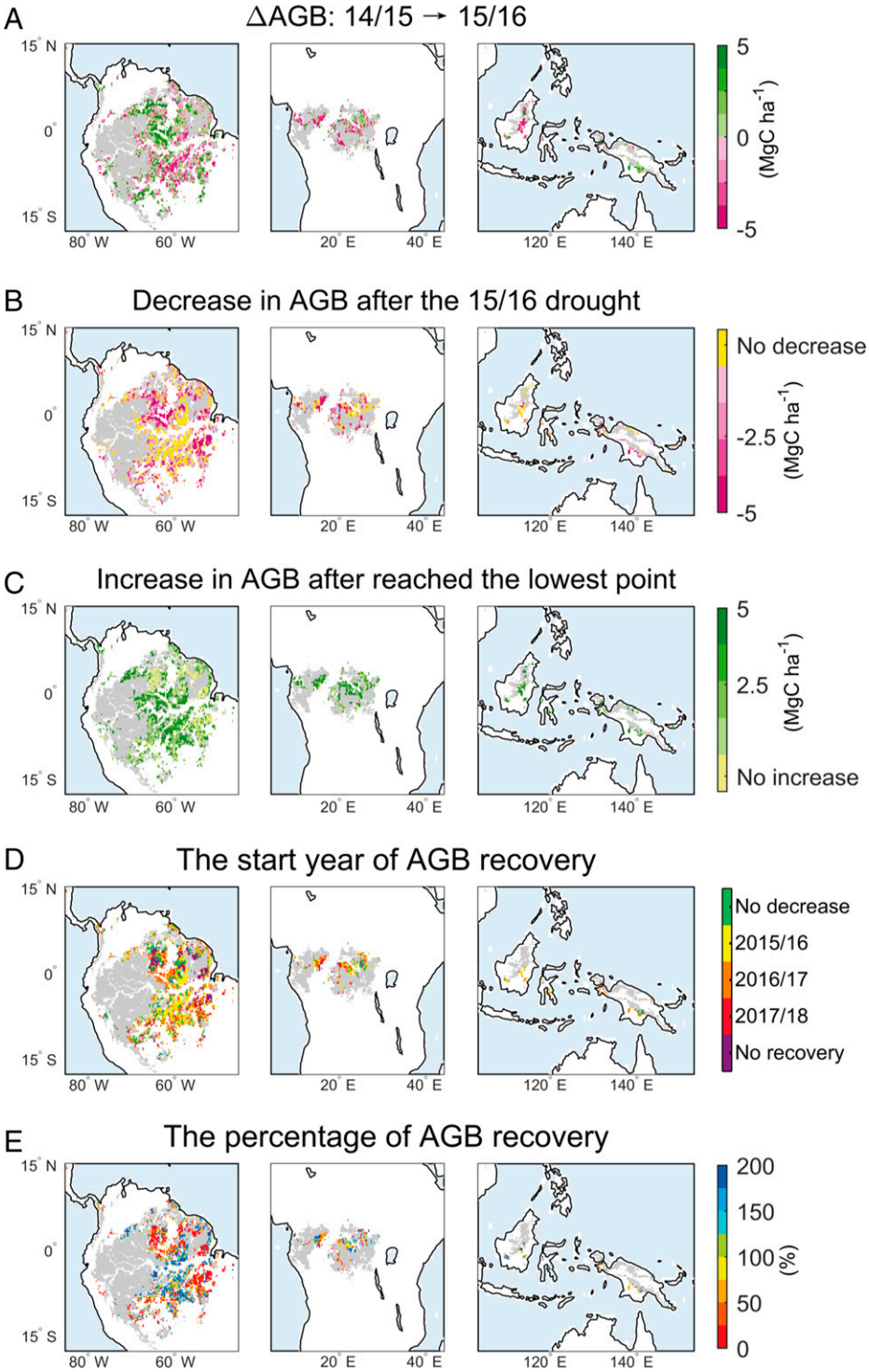


**Fig. 2.** Spatial patterns of forest AGB changes during and after the drought. (*A*) Changes in AGB over the drought period in 2015/16, relative to AGB over the same period in 2014/15 ($\Delta AGB_{14/15 \rightarrow 15/16}$). (*B*) Decreases in AGB after the drought. (*C*) Increases in AGB after reached the lowest AGB point. (*D*) The start year of AGB recovery, which is also the year with the lowest AGB value. Green areas correspond to areas where AGB has not reduced over the period of 2015 and 2017. Yellow areas correspond to areas where AGB in 2015/16 was the lowest and regrows immediately after the drought. Purple areas correspond to areas where AGB has not started to recover by 2019. (*E*) The percentage of AGB recovery—that is, the increase in AGB after the lowest point divided by the sum of decrease in AGB during and/or after the drought. The gray areas are the areas where the ACWD is greater than −1 (i.e., non-drought-affected region).

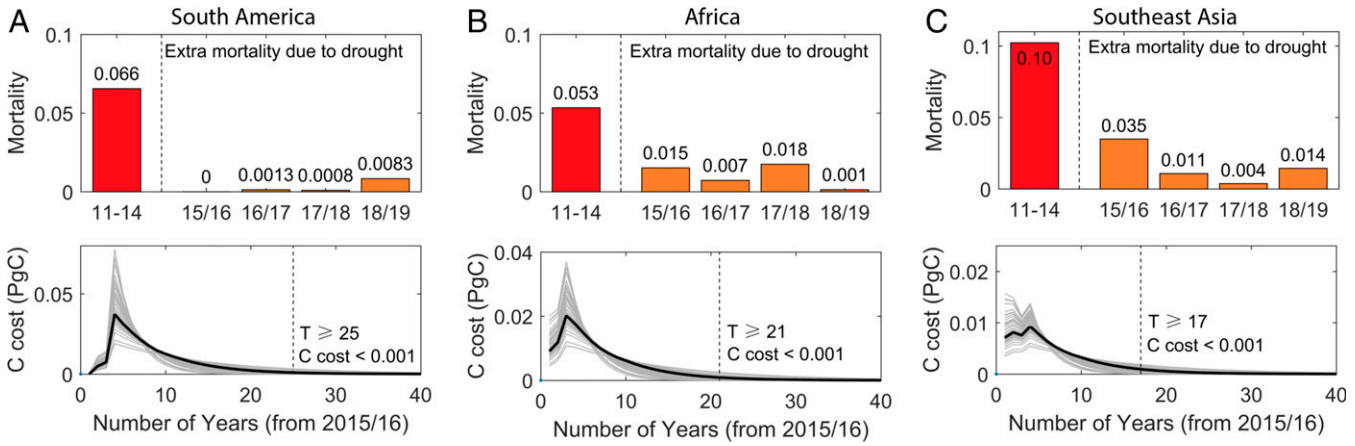


**Fig. 3.** Mortality rate and carbon cost from mortality over the drought-affected regions in South America (*A*), Africa (*B*), and Southeast Asia (*C*). *Upper* shows the averaged mortality rate during the period of 2011 through 2014 (red bar) and the extramortality rate (orange bars) in the drought year of 2015/16 and in the following years. *Lower* shows carbon cost from drought-induced extramortality. Gray curves present the estimates of carbon cost using different decomposition rate *k* from plot measurement. The black curve is the median value of all the estimates. The dashed vertical line indicates the number of years when carbon cost < 0.0001 PgC.

over intact forests in the epicenter of the 2005 drought in the Western Amazon (28, 29). The 2015/16 drought in regions with a lagged decrease of AGB has distinct features of high intensity and long duration, so that available soil water after the drought may have remained limiting and suppressed vegetation growth, through hydraulic failure or loss of nonstructural carbohydrates (30). On the other hand, after having reached the lowest AGB point, the trend of AGB reversed, and we find that more than 80% of the regions where AGB losses occurred had a reversal of AGB before 2019 (Fig. 2*C*). Divergent post-drought recovery trajectories are also evident. Some forests regrew short after the drought of 2015/16, whereas others declined in a few subsequent years. As shown in Fig. 2*D* and *SI Appendix*, Fig. S6, quick-recovering forests correspond roughly to those previously exposed to moderate or light drought, in eastern Amazonia, most parts of Africa, and Southeast Asia. Conversely, late-recovering forests are in south-central Amazonia, where the drought was more severe. The regions where AGB started to recover earlier also show a higher recovery level (Fig. 2*E*). By 2019, over about 40% of intact forests where AGB decreased had fully recovered to their predrought AGB level. The regions where AGB did not show any recovery or did not fully recover in 2019 include regions in the epicenter of the drought—north-central Amazonian forests, as well as the drier eastern Amazonia and western African regions near the edge of the intact tropical forest biome. Trees near forest edges are most likely more vulnerable to fires, canopy drying, and degradation (31), which could favor tree mortality and suppress AGB recovery.

We use a simple box model driven by our estimates of AGB changes, MODIS NPP product (i.e., MOD17A3HGF), MODIS leaf area index (LAI) product (i.e., MOD15A2), and NPP allocation fractions from Yang et al. (32), with specific leaf area from Butler et al. (33), to estimate the drought-induced extra mortality up to 2019 (see details in *SI Appendix*, Text S2 and Fig. 3). The drought-related tree mortality could occur years or even decades after drought event (10). We also noted that forest mortality does not cause an instantaneous emission of $CO_2$ to the atmosphere, but, rather, a lagged emission from decaying coarse woody debris (23). To assess the persistent impacts of drought-induced forest mortality on $CO_2$ emission, we use a first-order kinetics model to simulate the decomposition of coarse woody debris (see details in *SI Appendix*, Text S2 and Fig. S7). Our results show that the impacts of drought-induced mortality on carbon emissions over the whole tropics can last for more than 17 y. In South America, we inferred that coarse woody debris decay will continue to increase the atmospheric $CO_2$ during a period of up to 25 y (Fig. 3).

**Factors Influencing AGB Changes During and After Drought.** The factors that determine AGB changes during drought and its subsequent trajectory are complex and can be related to both exposure and vulnerability of forests. We use RF models (34) (*Materials and Methods*) to investigate the importance of more than 20 factors, including drought characteristics, background climate, soil properties, forest structure, and fire occurrence (*SI Appendix*, Table S1). Altogether, these factors explain 52% of the spatial variation of the observed changes in AGB during drought ($\Delta AGB_{14/15\rightarrow15/16}$; Fig. 4*A*) and 39% of the variation of the observed percentage of AGB recovery relative to previous losses of AGB (log-transformed) (Fig. 4*B*). The RF models present good predictive skills in reproducing the observed spatial patterns of AGB changes during drought and their relative recovery (*SI Appendix*, Fig. S8). Despite biases in predicting locally the recovery percentage, the RF model properly identified the regions with full versus incomplete recovery, with an accuracy of 93% (*SI Appendix*, Fig. S9 and confusion matrix in Table S2). Partial dependence plots for the six most influential factors in each RF model were calculated to examine the nonlinear dependence of AGB changes on different predictors, as shown in Fig. 4.

***AGB changes during the drought.*** Fig. 4*A* shows that soil-moisture changes during the drought year ($\Delta SM_{14/15\rightarrow15/16}$) is the most influential factor associated with AGB changes of $\Delta AGB_{14/15\rightarrow15/16}$. Unsurprisingly, larger soil-moisture deficits relative to the predrought level are associated with larger losses of AGB during the drought. A previous study suggested that these losses during drought were mainly driven by large mortality increases, rather than by declines in growth (2). High soil clay content is also strongly positively associated with the reduction of AGB during drought. We examined the covariation between soil clay content and $\Delta SM_{14/15\rightarrow15/16}$ (*SI Appendix*, Fig. S10) and the respective effects of these two drivers on $\Delta AGB_{14/15\rightarrow15/16}$ (*SI Appendix*, Fig. S11). This analysis confirmed that the impact of soil clay content on $\Delta AGB_{14/15\rightarrow15/16}$ is not an artifact, as $\Delta AGB_{14/15\rightarrow15/16}$

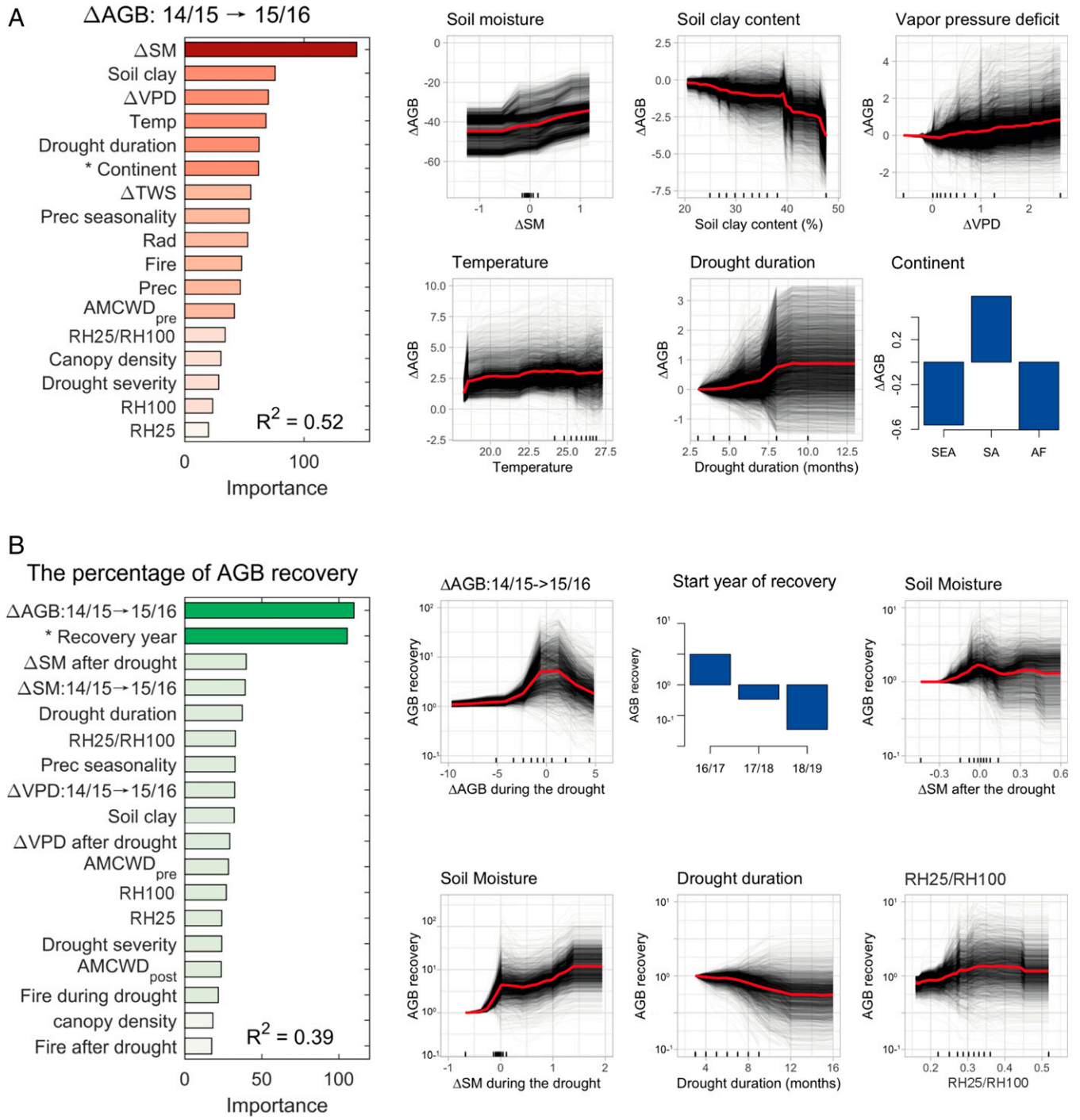


**Fig. 4.** The factors influencing AGB changes during and after the drought. (*A*) The importance of predictor variables to fit the AGB changes during the drought ($\Delta AGB_{14/15\rightarrow15/16}$) and the partial dependence plot of the top six variables. In the partial dependence plot, the red line is the partial dependence curve, showing the marginal effect of one given predictor variable on $\Delta AGB_{14/15\rightarrow15/16}$, averaged over all observed values of the other predictor variables. Black lines are the individual conditional expectation curves, displaying the dependence of $\Delta AGB_{14/15\rightarrow15/16}$ on corresponding predictor variables for each pixel instance separately. And rungs on the *x* axis show the deciles of the distribution of the predictors. (*B*) Same as *A*, but to fit the log-transformed percentage of AGB recovery after drought (exclude no recovery pixels). The predictors in bold in *B* are the factors also strongly associated with $\Delta AGB_{14/15\rightarrow15/16}$ in *A*.

decreased from low to high soil clay content areas for the same level of $\Delta SM_{14/15\rightarrow15/16}$. Two possible mechanisms may explain why a higher soil clay content associates with a larger AGB reduction during drought. First, the higher wilting point of clay-rich soils limits soil moisture available for plant roots (35). Second, the higher nutrient availability in clay soils may play a detrimental role during drought, as forests growing in clay soils with a larger content in nutrients—in particular, phosphorus—may be adapted to a higher nutrient use, leading to a higher embolism risk when severe water stress happens (36–38). The RF model also indicates that a longer drought duration was associated with an AGB increase during the drought year in the ever-wet north-central Amazonia (Figs. 1*B* and 2*A*). This is likely because in this region, background water availability is always high, and trees have deep rooting systems, being able to access groundwater. Our RF models also indicate that a higher VPD is associated with an increase of AGB during drought. A possible reason is that in the ever-wet tropics, increasing intrinsic water-use efficiency coincident with

higher radiation may sustain high photosynthesis, despite stomatal closure at high VPD levels, at least as long as soil moisture is not drawn down to levels approaching the wilting point (27, 39). Background mean annual temperature had a limited and positive effect on AGB response during drought. This result is consistent with results from space-for-time substitution, which suggests a limiting long-term effect of high temperatures on photosynthesis (40), carbon stocks, and carbon turnover rate (41).

***AGB recovery.*** As shown in Fig. 4*B*, the change of AGB during the drought year was the factor most strongly associated with the percentage of subsequent AGB recovery, according to our RF models. Pixels with a more negative $\Delta AGB_{14/15\rightarrow15/16}$ are generally associated with no legacy decrease after the drought, so that the minimum of AGB was reached just after the drought period. The partial dependence graphs in Fig. 4*B* show that more losses of AGB during drought are, nevertheless, associated with a lower recovery percentage (recovery percentage was calculated as the increase in AGB after the lowest AGB point divided by the sum of decreases in AGB during and after the drought; *Materials and Methods*). Conversely, the regions with positive $\Delta AGB_{14/15\rightarrow15/16}$ during drought in the ever-wet central Amazon tend to show legacy losses after the drought and a lower recovery (Fig. 4*B*). Thus, the AGB change during the drought was a strong predictor of the postdrought AGB recovery. Soil moisture changes during the drought year ($\Delta SM_{14/15\rightarrow15/16}$), which was the strongest predictor of the AGB response during drought, were also positively associated with the percentage of AGB recovery (Fig. 4*B*). Locally, a longer drought was associated with a lower recovery level of AGB (Fig. 4*B*). Apart from those factors found to be influential for AGB changes during drought, the start year of the AGB recovery and soil-moisture changes after drought play the second and third most important role in explaining the postdrought AGB recovery percentage. The sooner forests start to recover, the higher recovery percentage they can reach within the observed time frame.

In addition, we found that the $\gamma$, defined as the ratio of 25% energy return height (RH25) to 100% energy return height (RH100) from satellite Lidar data (42), was also positively associated with the recovery of AGB after the drought. In Fig. 5, we compared the start year of recovery and the mean annual AGB recovery rate between high-$\gamma$ ($\geq 0.3$) and low-$\gamma$ ($< 0.3$) forests for different levels of soil water deficits. In all cases, forests with a high $\gamma$ appear to have a stronger capacity to recover than low-$\gamma$ ones. To isolate the factors influencing $\gamma$, we assessed the relation of $\gamma$ with RH25 and RH100, respectively. We found that $\gamma$ increases significantly with RH25, rather than with RH100, especially when RH100 > 20 m (*SI Appendix*, Fig. S12). Here, both RH25 and RH100 extracted from Lidar waveforms reflect the structure of forests, but the underlying mechanism behind spatial changes in $\gamma$ is still unclear. We proposed three possible explanations: 1) A high $\gamma$ may reflect factors with a tall understory; 2) a high $\gamma$ may reflect forests with a dense (thick) and closed canopy because Lidar photons penetrate less into dense canopies and do not probe the understory structure; or 3) a high $\gamma$ may relate to intact forests and a low $\gamma$ may reflect degraded forests. In the Amazon, forests and low $\gamma$ ($< 0.3$) are, in fact, geographically overlapping with degradation-affected forests (*SI Appendix*, Fig. S13). Thus, a low $\gamma$ may be a consequence of forest degradation. To examine this hypothesis, we assessed the probability density functions of $\gamma$ of Amazonian forests with and without degradation, according to the degradation map of ref. 43. We found that degraded forests (especially from fires and fragmentation) have significantly lower $\gamma$ compared to intact forests (*SI Appendix*, Fig. S13). These findings reflect the importance of accounting for forest structure, including its alteration by degradation, when predicting the tropical forest dynamics after droughts. Future research could compare the resilience of degraded versus intact forests to droughts.

## Conclusions

AGB changes of intact tropical forests during the 2015/16 drought, both positive and negative, depending upon regions, are associated with drought severity (soil water deficit) and duration, as well as with soil clay content. The AGB recovery after the drought was influenced by previous AGB losses, modulated by climatic water deficit, soil clay fraction, and forest structure. Our results shed light on the attribution of AGB changes during and after droughts to different drivers, showing that predicting the long-term impact of drought on forest communities is more challenging because drought influences demographic processes beyond immediate growth and mortality during the water-deficit period. The driving role of forest structure on recovery suggests compensatory responses of taller trees versus understory, which need to be confirmed by ground-based inventories and drought experiment results. Moreover, as climate change is expected to produce more compound, frequent, severe, and long-lasting

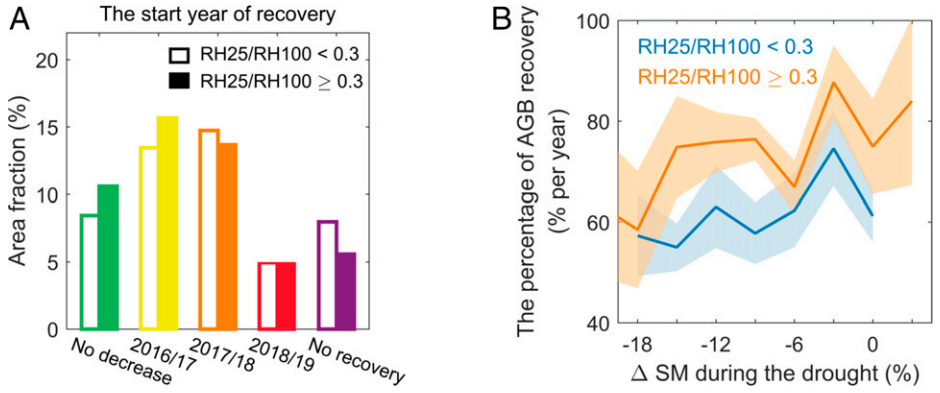


**Fig. 5.** The start year of AGB recovery and the rate of AGB recovery for canopy-closed forests and low understory forests. (*A*) The fraction of study area (%) with a different start year of AGB recovery of canopy-closed forests, where the understory height is close to the top canopy height ($\gamma \geq 0.3$), and forests with low understory ($\gamma < 0.3$). (*B*) The median of the percentage of AGB recovery per year (% per year) of forests for different levels of soil-moisture (SM) deficits during the drought year.

tropical drought events in the future (44, 45), a better understanding of the response and recovery of tropical forest dynamics during and after the drought can provide valuable information for the climate-modeling community, in order to more accurately predict ecosystem response to drought events under future climate scenarios.

## Materials and Methods

**L-VOD AGB.** Satellite-based L-VOD data at 25- × 25-km resolution covering the period from 2010 to 2019 from the SMOS (SMOS-IC, version 2) satellite is used for the analysis. The method used here to compute AGB from L-VOD in the same as the method used in refs. 8, 46, and 47; that is, we use four different static AGB benchmark maps to calibrate the relationship between L-VOD and AGB for the entire tropical region, South America, and Africa separately. The calibration process for only Southeast Asia is not used because of the limited SMOS observations in this region. The AGB benchmark maps include three pantropical maps (i.e., refs. 48–50) and one map covering only Africa (51). After the calibration, 10 maps of L-VOD AGB can be obtained, and the median of these 10 maps of monthly L-VOD AGB covering the period of 2010 through 2018 is used in this study. Fan et al. (47) have assessed the uncertainty of AGB changes derived from L-VOD, which includes internal uncertainty from transferring the L-VOD to AGB and external uncertainty from different reference biomass maps. In total, the uncertainty of L-VOD–derived AGB data was on the order of 20 to 30% over tropics. Because of the poor quality of L-VOD data over the water bodies, we remove the 25-km pixels where the areal fraction of regularly flooded wetlands is more than 80%, using a global wetland map from ref. 52.

**Forest Cover Mask.** In this study, we focus on the tropical intact evergreen forests (between 25°N and 25°S), which are defined by the European Space Agency (ESA) Climate Change Initiative (CCI) land-cover map of 2015 (300-m resolution), Hansen forest-cover map of the year 2000, and the annual deforestation maps from 2000 to 2018 (25-m resolution) (53). First, using the 300-m resolution CCI land-cover map, we label the 25-km pixel dominated by evergreen forest, in which more than 50% of the 300-m-sized pixels are evergreen forests (classes ID 50, 160, and 170). Second, for each 25-km pixel, we calculate the percentage of the 25-m pixels with a forest cover lower than 90% or affected by deforestation, using the Hansen tree-cover map. The 25-km pixels with a forest cover < 90% or deforestation higher than 20% are removed.

**Drought Characteristics.** The Cumulative Water Deficit (CWD) is widely used to describe the characteristics of "meteorologically induced" drought in the tropics (54). Based on precipitation data from NASA's TRMM (monthly, 0.25° resolution, TMPA/3B43 v7) and ET data from GLEAM (monthly, 0.25° resolution, v3.3a), we calculate monthly CWD for each pixel, as follows:

$$CWD_m = CWD_{m-1} - E_m + P_m \quad \text{if } CWD_m < 0$$
$$CWD_m = 0 \quad \text{if } CWD_m \geq 0,$$

where $CWD_m$ is the CWD of the current month, which is equal to the CWD from previous months ($CWD_{m-1}$) plus the difference between the precipitation of the current month ($P_m$) and ET ($E_m$). For each grid cell, the ACWD at the $i$th grid for the $t$th month ($t = 1,2,\ldots,12$) is calculated as:

$$ACWD_{i,t} = \frac{CWD_{i,t} - \overline{CWD_{i,t}}}{\sigma(CWD_{i,t})},$$

where $\overline{CWD_{i,t}}$ and $\sigma(CWD_{i,t})$ are the mean value and SD of $CWD$ at the $i$th grid for the $t$th month during the reference period (2000 through 2019).

We use the monthly ACWD to identify the spatial extent, duration, severity, onset, and end of the 2015/16 drought in the tropical forest. For each grid cell, the ACWD is smoothed by using the 3-mo running average to avoid a single wet month interrupting a long and consecutive dry period. The drought events that last a short time (i.e., duration < 3 mo) are not included in this study. The drought onset is defined as the first month with ACWD below the threshold of −1 SD, and the drought end is defined as the first month when ACWD up-crosses the threshold of −1 SD. We also derive the duration of drought as the period between the start and the end months of the drought event and the severity of drought as the median of ACWD during the drought period.

**AGB Response and Recovery.** This study and Wigneron et al. (8) used the same quantity L-VOD AGB from the same satellite. In this study, to filer AGB changes during the nondrought months of 2015/16, we calculated the averages of monthly AGB during the drought period, rather than the annual mean AGB (see details in *SI Appendix*, Text S3). We calculate the average of monthly L-VOD AGB for the whole drought period; for example, the start month of the drought event is October (Oct) 2015 and the end is March (Mar) 2016, and $AGB_{15/16} = \overline{AGB_i}$ ($i$ = Oct, November, and December 2015 and January, February, and Mar 2016). The responses of AGB during drought are calculated as the averages of AGB stocks during the 2015/16 drought period minus the averages of AGB stocks for the same months, but during the years 2014 and 2015 ($\Delta AGB_{14/15\rightarrow15/16}$):

$$\Delta AGB_{14/15\rightarrow15/16} = AGB_{15/16} - AGB_{14/15}.$$

We also calculate the average of AGB for the same months, but during the years 2016/17, 2017/18, and 2018/19. The decrease and increase in AGB after drought are calculated as:

$$\text{Decrease in AGB after drought} : AGB_{min} - AGB_{15/16},$$
$$\text{Increase in AGB after drought} : AGB_{max} - AGB_{min},$$

where $AGB_{min}$ is the minimum value among $AGB_{15/16}$, $AGB_{16/17}$, $AGB_{17/18}$, and $AGB_{18/19}$; $AGB_{max}$ is the maximum value of AGB after reaching the $AGB_{min}$; and the percentage of AGB recovery is the ratio of increase in AGB after the drought and the sum of decrease in AGB during and after the drought, calculated as:

$$\text{The percentage of AGB recovery} : \frac{AGB_{max} - AGB_{min}}{AGB_{14/15} - AGB_{min}}.$$

**Variable Importance and Partial Dependence.** To fit the AGB response during drought and recovery after drought, we use more than 20 predictor variables, including drought characteristics, background climate, soil property, forest structure, fire occurrence, and two categorical variables (*SI Appendix*, Table S1).

The predictor variables of drought characteristics used are predrought ACWD ($ACWD_{pre}$), postdrought ACWD ($ACWD_{post}$), drought severity, drought duration, soil moisture (SM), and VPD anomalies during drought and after the drought. Soil-moisture data are from the SMOS-IC satellite. VPD is calculated by using reanalysis climate products from the Modern-Era Retrospective Analysis for Research and Applications,

$$VPD = SVP - AVP,$$
$$SVP = 0.6108 \times e^{\frac{17.27\times T_a}{237.3+T_a}},$$
$$AVP = SVP \times \frac{RH}{100},$$

where $SVP$ and $AVP$ are saturated vapor pressure and actual vapor pressure (kPa), $T_a$ is air temperature at 2 m (°C), and $RH$ is relative humidity at 2 m (%). The predictor variables of background climate used are the average of temperature, precipitation, and radiation during the drought period and precipitation seasonality (SD of 12-mo precipitation). The climatological monthly temperature, precipitation, and radiation are from the WorldClim database (https://www.worldclim.org). The predictor variables of soil property are soil clay content (%) from SoilGrids (https://soilgrids.org). The predictor variables of forest structure from the Geoscience Laser Altimeter System aboard the Ice, Cloud, and Land Elevation Satellite (https://nsidc.org/data/icesat) are canopy density (the proportion of an area in the ground that is covered by the crown of trees), canopy height (RH100), understory height (RH25), and the ratio of understory and canopy height (RH25/RH100). The predictor variable of the occurrence of fire disturbance is fire radiative power (FRP) observations from the Global Fire Assimilation System (55). In addition, two categorical variables are Continent (SA, AF, and SEA for South America, Africa, and Southeast Asia, respectively) and the start of the recovery year (15/16, 16/17, and 17/18).

We use RF models to quantify how important each predictor variable is in determining the fitted values of $\Delta AGB_{14/15\rightarrow15/16}$ and the percentage of AGB recovery. The RF model is a popular supervised learning algorithm (34, 56). It operates by constructing a multitude of decision trees from a training dataset. Each tree is trained on a random subset of data, and the results of all the decision trees are then combined to give a final prediction. Model performances were assessed with the mean absolute error (MAE) and the $R^2$ value. The selected model has the smallest MAE and the highest $R^2$. The spatial patterns of the RF-predicted values are compared with the observed values (*SI Appendix*, Fig. S8). Additionally, the observed recovery percentage could be classified into

two categories, namely, with recovery percentage less than 100% and equal to/greater than 100%. We also test if the above-mentioned RF-predicted recovery percentage can be classified into the proper category (*SI Appendix*, Fig. S9 and Table S2). Partial dependence plots based on the RF algorithm are used to visualize the relationship between predictor variables and $\Delta AGB_{14/15\rightarrow15/16}$ (or the percentage of AGB recovery), independent of other predictor variables. This is the marginal effect of one predictor variable on AGB changes, not the absolute value of changes in AGB. The predictor variables with flat response functions–-that is, no change in AGB response and recovery with the predictor variable–are typically relatively unimportant.

We also use the multiple linear regression model for validity. For AGB changes during the drought ($\Delta AGB_{14/15\rightarrow15/16}$), two variables–i.e., canopy height and RH25/RH100–are excluded in the best multiple linear regression model, according to the Akaike Information Criterion (AIC) statistic. These two variables also show low importance in our RF model (Fig. 4*A*). The best multiple linear regression model can explain only 7.8% of variations in $\Delta AGB_{14/15\rightarrow15/16}$ ($R^2 = 0.078$). The Variance Inflation Factor (VIF) of all the predictors is less than 2.5, suggesting no multicollinearity. Finally, we check the residual plot of fitted values versus the residuals, which imply a problem with the linear assumption of the model (*SI Appendix*, Fig. S14*A*). Thus, using an RF model to predict $\Delta AGB_{14/15\rightarrow15/16}$ is necessary. For the AGB recovery rate, only eight variables are kept in the best multiple linear regression model, according to the AIC statistic. Among these eight predictors, six of them have significant coefficients, according to the *t*-statistic test ($P < 0.05$), including $\Delta AGB_{14/15\rightarrow15/16}$, Recovery year, $\Delta SM_{14/15\rightarrow15/16}$, Drought duration, RH25/RH100, and fire after drought. Five out of six predictors (except for fire after drought) show high importance in our RF model (Fig. 4*B*). This best multiple linear regression model can explain 19.3% of variations in the log-transformed percentage of AGB recovery after drought ($R^2 = 0.193$, less than the $R^2$ of the RF model). The VIF of all the predictors is less than two, and the residual plot shows no problem with the linear assumption of model (*SI Appendix*, Fig. S14*B*). Using multiple linear regression to predict AGB recovery rate is possible, but its prediction capacity is lower than the RF model.

**Data Availability.** The authors declare that all methods needed to evaluate the conclusions in the paper are present in *Materials and Methods* and/or the supporting information. The following previously published data were used in this work: TRMM 3B43 rainfall (57), GLEAM ET (58), ESA CCI land cover map (59), Hansen global forest change data (60), MODIS NPP (MOD17A3HGF) (61), MODIS LAI (MOD15A2) (62), Global map of plant trait distribution (63), and L-VOD AGB data (64). The computer codes and data used for this analysis are publicly available in Figshare.

**ACKNOWLEDGMENTS.** This research has been funded by the European Space Agency (ESA) as part of the CCI Biomass project of the Climate Change Initiative (ESA ESRIN/Contract Number 4000123662).

Author affiliations: [a]Laboratoire des Sciences du Climat et de l'Environnement, Institut Pierre-Simon Laplace, Commissariat à l'Énergie Atomique et aux Énergies Alternatives-CNRS-Université de Versailles Saint-Quentin-en-Yvelines, Université Paris-Saclay, 91191 Gif-sur-Yvette, France; [b]Interactions Soil Plant Atmosphere (ISPA), UMR 1391, Institut National de Recherche pour l'Agriculture l'Alimentation et l'Environnement (INRAE), Nouvelle-Aquitaine,Villenave d'Ornon, 33140 France; [c]Laboratoire Evolution et Diversité Biologique, Université Paul Sabatier, 31062 Toulouse, France; [d]Gamma Remote Sensing, Worbstrasse 225, Gümligen, 3073 Switzerland; [e]Guangdong Province Key Laboratory for Climate Change and Natural Disaster Studies, School of Atmospheric Sciences, Sun Yat-sen University, Guangzhou 510275, China; [f]Chongqing Jinfo Mountain Karst Ecosystem National Observation and Research Station, School of Geographical Sciences, Southwest University,Chongqing, 400715 China; [g]Oceans and Atmosphere, Commonwealth Scientific and Industrial Research Organisation, Aspendale, VIC 3195, Australia; [h]Centre National de Recherches Météorologiques, Université de Toulouse, Météo-France, CNRS, 31057 Toulouse, France; [i]Department of Geography and Earth Sciences, Aberystwyth University, Aberystwyth SY23 3FL, United Kingdom; and [j]Institut National de la Recherche Agronomique, Université Paris-Saclay, AgroParisTech, UMR 518 MIA, Palaiseau, 91120 France

1. Y. Pan *et al.*, A large and persistent carbon sink in the world's forests. *Science* **333**, 988–993 (2011).
2. O. L. Phillips *et al.*, Drought sensitivity of the Amazon rainforest. *Science* **323**, 1344–1347 (2009).
3. R. Seidl *et al.*, Forest disturbances under climate change. *Nat. Clim. Chang.* **7**, 395–402 (2017).
4. R. J. Brienen *et al.*, Long-term decline of the Amazon carbon sink. *Nature* **519**, 344–348 (2015).
5. E. T. A. Mitchard, The tropical forest carbon cycle and climate change. *Nature* **559**, 527–534 (2018).
6. J. Liu *et al.*, Contrasting carbon cycle responses of the tropical continents to the 2015-2016 El Niño. *Science* **358**, eaam5690 (2017).
7. C. Rödenbeck, S. Zaehle, R. Keeling, M. Heimann, History of El Niño impacts on the global carbon cycle 1957-2017: A quantification from atmospheric $CO_2$ data. *Philos. Trans. R. Soc. Lond. B Biol. Sci.* **373**, 20170303 (2018).
8. J. P. Wigneron *et al.*, Tropical forests did not recover from the strong 2015-2016 El Niño event. *Sci. Adv.* **6**, eaay4603 (2020).
9. Y. Malhi, L. Rowland, L. E. O. C. Aragão, R. A. Fisher, New insights into the variability of the tropical land carbon cycle from the El Niño of 2015/2016. *Philos. Trans. R. Soc. Lond. B Biol. Sci.* **373**, 20170298 (2018).
10. C. D. Allen *et al.*, A global overview of drought and heat-induced tree mortality reveals emerging climate change risks for forests. *For. Ecol. Manage.* **259**, 660–684 (2010).
11. T. J. Brodribb, J. Powers, H. Cochard, B. Choat, Hanging by a thread? Forests and drought. *Science* **368**, 261–266 (2020).
12. S. W. Rifai *et al.*, ENSO Drives interannual variation of forest woody growth across the tropics. *Philos. Trans. R. Soc. Lond. B Biol. Sci.* **373**, 20170410 (2018).
13. Y. Malhi *et al.*, The linkages between photosynthesis, productivity, growth and biomass in lowland Amazonian forests. *Glob. Change Biol.* **21**, 2283–2295 (2015).
14. V. A. H. F. Dos Santos *et al.*, Causes of reduced leaf-level photosynthesis during strong El Niño drought in a Central Amazon forest. *Glob. Change Biol.* **24**, 4266–4279 (2018).
15. A. Shenkin *et al.*, Interactive effects of tree size, crown exposure and logging on drought-induced mortality. *Philos. Trans. R. Soc. Lond. B Biol. Sci.* **373**, 20180189 (2018).
16. B. Martens *et al.*, GLEAM v3: Satellite-based land evaporation and root-zone soil moisture. *Geosci. Model Dev.* **10**, 1903–1925 (2017).
17. J. P. Wigneron *et al.*, Modelling the passive microwave signature from land surfaces: A review of recent results and application to the L-band SMOS & SMAP soil moisture retrieval algorithms. *Remote Sens. Environ.* **192**, 238–262 (2017).
18. A. G. Konings, K. Rao, S. C. Steele-Dunne, Macro to micro: Microwave remote sensing of plant water content for physiology and ecology. *New Phytol.* **223**, 1166–1172 (2019).
19. L. Rowland *et al.*, Death from drought in tropical forests is triggered by hydraulics not carbon starvation. *Nature* **528**, 119–122 (2015).
20. C. E. Doughty *et al.*, Drought impact on forest carbon dynamics and fluxes in Amazonia. *Nature* **519**, 78–82 (2015).
21. A. T. Trugman *et al.*, Tree carbon allocation explains forest drought-kill and recovery patterns. *Ecol. Lett.* **21**, 1552–1560 (2018).
22. S. R. Saleska *et al.*, Dry-season greening of Amazon forests. *Nature* **531**, E4–E5 (2016).
23. P. M. Brando *et al.*, Abrupt increases in Amazonian tree mortality due to drought-fire interactions. *Proc. Natl. Acad. Sci. U.S.A.* **111**, 6347–6352 (2014).
24. K. Guan *et al.*, Photosynthetic seasonality of global tropical forests constrained by hydroclimate. *Nat. Geosci.* **8**, 284–289 (2015).
25. J. Wu *et al.*, Leaf development and demography explain photosynthetic seasonality in Amazon evergreen forests. *Science* **351**, 972–976 (2016).
26. X. Chen *et al.*, Novel representation of leaf phenology improves simulation of Amazonian evergreen forest photosynthesis in a land surface model. *J. Adv. Model. Earth Syst.* **12**, e2018MS001565 (2020).
27. J. K. Green, J. Berry, P. Ciais, Y. Zhang, P. Gentine, Amazon rainforest photosynthesis increases in response to atmospheric dryness. *Sci. Adv.* **6**, eabb7232 (2020).
28. S. Saatchi *et al.*, Persistent effects of a severe drought on Amazonian forest canopy. *Proc. Natl. Acad. Sci. U.S.A.* **110**, 565–570 (2013).
29. Y. Yang *et al.*, Post-drought decline of the Amazon carbon sink. *Nat. Commun.* **9**, 3172 (2018).
30. C. Signori-Müller *et al.*, Non-structural carbohydrates mediate seasonal water stress across Amazon forests. *Nat. Commun.* **12**, 2310 (2021).
31. A. H. Rice *et al.*, Carbon balance and vegetation dynamics in an old-growth Amazonian forest. *Ecol. Appl.* **14**, 55–71 (2004).
32. H. Yang *et al.*, Variations of carbon allocation and turnover time across tropical forests. *Glob. Ecol. Biogeogr.* **30**, 1271–1285 (2021).
33. E. E. Butler *et al.*, Mapping local and global variability in plant trait distributions. *Proc. Natl. Acad. Sci. U.S.A.* **114**, E10937–E10946 (2017).
34. L. Breiman, Random forests. *Mach. Learn.* **45**, 5–32 (2001).
35. R. J. Fensham, D. W. Butler, J. Foley, How does clay constrain woody biomass in drylands? *Glob. Ecol. Biogeogr.* **24**, 950–958 (2015).
36. A. Gessler, M. Schaub, N. G. McDowell, The role of nutrients in drought-induced tree mortality and recovery. *New Phytol.* **214**, 513–520 (2017).
37. J. L. Soong *et al.*, Soil properties explain tree growth and mortality, but not biomass, across phosphorus-depleted tropical forests. *Sci. Rep.* **10**, 2302 (2020).
38. R. S. Oliveira *et al.*, Linking plant hydraulics and the fast-slow continuum to understand resilience to drought in tropical ecosystems. *New Phytol.* **230**, 904–923 (2021).
39. Q. Zhang *et al.*, Response of ecosystem intrinsic water use efficiency and gross primary productivity to rising vapor pressure deficit. *Environ. Res. Lett.* **14**, 074023 (2019).
40. M. Huang *et al.*, Air temperature optima of vegetation productivity across global biomes. *Nat. Ecol. Evol.* **3**, 772–779 (2019).
41. M. J. P. Sullivan *et al.*, Long-term thermal sensitivity of Earth's tropical forests. *Science* **368**, 869–874 (2020).
42. D. J. Harding, C. C. Carabajal, ICESat waveform measurements of within-footprint topographic relief and vegetation vertical structure. *Geophys. Res. Lett.* **32**, L21S10 (2005).
43. E. A. T. Matricardi *et al.*, Long-term forest degradation surpasses deforestation in the Brazilian Amazon. *Science* **369**, 1378–1382 (2020).
44. S. Seveviratne *et al.*, "Changes in climate extremes and their impacts on the natural physical environment" in *Managing the Risks of Extreme Events and Disasters to Advance Climate Change Adaptation: Special Report of the Intergovernmental Panel on Climate Change*, C. B. Field *et al.*, Eds. (Cambridge University Press, Cambridge, UK, 2012), pp. 109–230.
45. J. Zscheischler *et al.*, Future climate risk from compound events. *Nat. Clim. Chang.* **8**, 469–477 (2018).
46. M. Brandt *et al.*, Satellite passive microwaves reveal recent climate-induced carbon losses in African drylands. *Nat. Ecol. Evol.* **2**, 827–835 (2018).
47. L. Fan *et al.*, Satellite-observed pantropical carbon dynamics. *Nat. Plants* **5**, 944–951 (2019).
48. S. S. Saatchi *et al.*, Benchmark map of forest carbon stocks in tropical regions across three continents. *Proc. Natl. Acad. Sci. U.S.A.* **108**, 9899–9904 (2011).

49. V. Avitabile *et al.*, An integrated pan-tropical biomass map using multiple reference datasets. *Glob. Change Biol.* **22**, 1406–1420 (2016).
50. A. G. S. J. Baccini *et al.*, Estimated carbon dioxide emissions from tropical deforestation improved by carbon-density maps. *Nat. Clim. Chang.* **2**, 182–185 (2012).
51. A. Bouvet *et al.*, An above-ground biomass map of African savannahs and woodlands at 25 m resolution derived from ALOS PALSAR. *Remote Sens. Environ.* **206**, 156–173 (2018).
52. A. Tootchi, A. Jost, A. Ducharne, Multi-source global wetland maps combining surface water imagery and groundwater constraints. *Earth Syst. Sci. Data* **11**, 189–220 (2019).
53. M. C. Hansen *et al.*, High-resolution global maps of 21st-century forest cover change. *Science* **342**, 850–853 (2013).
54. L. E. O. Aragão *et al.*, Spatial patterns and fire response of recent Amazonian droughts. *Geophys. Res. Lett.* **34**, L07701 (2007).
55. J. W. Kaiser *et al.*, Biomass burning emissions estimated with a global fire assimilation system based on observed fire radiative power. *Biogeosci.* **9**, 527–554 (2012).
56. K. P. Murphy, *Machine Learning: A Probabilistic Perspective* (The MIT Press, Cambridge, MA, 2012).
57. M.D. Greenbelt, Data from "Tropical Rainfall Measuring Mission (TRMM) (2011), TRMM (TMPA/3B43) rainfall estimate L3 1 month 0.25 degree x 0.25 degree V7." https://disc.gsfc.nasa.gov/datasets/TRMM_3B43_7/summary. Accessed 16 February 2020.
58. GLEAM, "Global Land Evaporation Amsterdam Model (GLEAM) v3.3." https://www.gleam.eu/#home. Accessed 20 October 2020.
59. European Space Agency, Data from "Download CCI LC Products." https://www.esa-landcover-cci.org/?q=node/164. Accessed 20 October 2020.
60. M. C. Hansen, et al., Data from "High-Resolution Global Maps of 21st-Century Forest Cover Change." http://earthenginepartners.appspot.com/science-2013-global-forest. Accessed 17 September 2020.
61. S. Running, M. Zhao. "MOD17A3HGF MODIS/Terra Net Primary Production Gap-Filled Yearly L4 Global 500 m SIN Grid V006. 2019." https://doi.org/10.5067/MODIS/MOD17A3HGF.006. Accessed 15 June 2022.
62. R. Myneni, Y. Knyazikhin, T. Park, Data from "MOD15A2–MODIS/Terra Leaf Area Index/FPAR 8-Day L4 Global 1km SIN Grid." https://ladsweb.modaps.eosdis.nasa.gov/missions-and-measurements/products/MOD15A2/. Accessed 26 September 2021.
63. E. Butler, et al. (2017). Mapping local and global variability in plant trait distributions. Proc. of the National Academy of Sciences, 114(51), E10937–E10946.
64. H. Yang, Data from "Climatic and biotic factors influencing regional declines and recovery of tropical forest biomass from the 2015/16 El Niño." Figshare. https://doi.org/10.6084/m9.figshare.19617894.v1. Accessed 28 March 2020.